



A re-evaluation of metal diapir breakup and equilibration in terrestrial magma oceans

Henri Samuel

Bayerisches Geoinstitut, Universität Bayreuth, Germany

ARTICLE INFO

Article history:

Received 16 September 2011
 Received in revised form 1 November 2011
 Accepted 3 November 2011
 Available online 9 December 2011

Editor: Y. Ricard

Keywords:

metal diapir
 breakup
 core formation
 magma ocean
 metal–silicate equilibration

ABSTRACT

Due to mechanisms such as impact heating, early atmospheric thermal blanketing, and radioactive heating, the presence of at least one global magma ocean stage in the early histories of terrestrial planets seems unavoidable. In such a context, a key question to constrain the early thermo–chemical evolution of the Earth is how much iron diapirs provided by differentiated impactors emulsified during their sinking towards the bottom of an early magma ocean.

In the past years, several workers have focused on this question, using however various approaches and making different assumptions. While most studies favor rapid breakup and equilibration of iron bodies during their sinking through the magma ocean, recent work suggests that iron bodies of size comparable or greater than a few tens of kilometers may preserve most of their initial volume as they reach the bottom of a magma ocean, therefore leading to metal–silicate disequilibrium.

To clarify the discrepancies and the differences among studies I have conducted a series of numerical simulations and theoretical calculations to derive the conditions and the timing for the breakup of metal diapirs of any size, sinking through a silicate magma ocean, with a large range of plausible viscosity values. The obtained breakup criterion is used to derive stable diapir sizes and their ability to equilibrate with the surrounding silicates. I show that for plausible magma ocean viscosities, diapirs with initial radii smaller than the thickness of a magma ocean rapidly break up into stable diapir sizes smaller than 0.2 m, at which metal–silicate equilibration is rapidly achieved.

© 2011 Elsevier B.V. All rights reserved.

1. Introduction

The earliest stages of planetary evolution are punctuated by a great variety of events that have reshaped the Earth and other terrestrial planets and influenced their long term evolution. During the accretional stages of planetary evolution, planetesimals driven by gravitational interactions aggregate rapidly into growing planetary embryos (Kokubo and Ida, 1996; Kortenkamp et al., 2000; Weidenschilling, 1976). Throughout the duration of the accretional growth period, physical processes, such as radioactive decay, impact heating, and possibly thermal blanketing, significantly contribute to increasing the protoplanet's temperature. Once the radius of the growing terrestrial planet reaches a critical size of about 1000 km, the kinetic energy provided by incoming planetesimals becomes large enough to trigger local melting (Coradini et al., 1983; Davies, 1985; Safronov, 1978; Sasaki and Nakazawa, 1986; Senshu et al., 2002; Tonks and Melosh, 1992). As inferred from N-body simulations, during the late stages of planetary accretion (oligarchic growth), impacts become more energetic (Kokubo and Ida, 1996), leading to more frequent melting events of greater extents. Moreover, the latest stages of planetary accretion are also characterized by the occurrence of giant impacts (Benz et al., 1986; Canup, 2004), followed by isostatic readjustment, which are expected to trigger global scale melting as well as possible vaporization on terrestrial planets

(Tonks and Melosh, 1993). The presence of a steamed impact-heated atmosphere would also favor the occurrence of large scale melting events (Abe, 1997). Therefore, with such an array of mechanisms favoring high temperatures, the occurrence of at least one global scale melting event during the early stages of terrestrial planet formation seems unavoidable (Tonks and Melosh, 1993).

In addition, radioactive heating produced by the disintegration of ^{26}Al and ^{60}Fe could also yield super-solidus temperatures, even in bodies of modest sizes such as planetesimals (Merk et al., 2002; Walter and Trønnes, 2004). Therefore, incoming impactors may have already been differentiated, with a small iron core surrounded by silicate material.

In such a context a key question is how much iron diapirs provided by differentiated impactors have emulsified during their sinking towards the bottom of an early magma ocean. Addressing this problem allows one to put strong constraints on metal–silicate equilibration processes (Dahl and Stevenson, 2010; Karato and Murthy, 1997; Rubie et al., 2003; Rubie et al., 2007; Wood et al., 2006). This is of prime importance for the interpretation of cosmochemical data such as Hf/W and U/Pb chronometers, allowing to put bounds on the timing of the accretion and differentiation of the Earth and other terrestrial bodies (Dahl and Stevenson, 2010; Kleine and Rudge, 2011; Kleine et al., 2004a; Kleine et al., 2004b; Rudge et al., 2010). In addition, the size of iron bodies sinking through the solid or molten silicate proto-mantle determines the heat distribution within a young terrestrial planet (Ichikawa et al., 2010; King and

E-mail address: henri.samuel@uni-bayreuth.de.

Olson, 2011; Lin et al., 2011; Monteux et al., 2009; Monteux et al., 2011; Ricard et al., 2009; Samuel et al., 2010; Senshu et al., 2002), which influences the subsequent long-term planetary thermal evolution.

Until recently, it was thought that even large iron diapirs sinking through a silicate magma ocean would rapidly break up into centimeter or millimeter-sized droplets (Ichikawa et al., 2010; Rubie et al., 2003; Stevenson, 1990). Such small droplets would allow metal-silicate equilibration to occur within sinking distances of just a few tens of meters (Karato and Murthy, 1997; Rubie et al., 2003). However, this scenario was recently questioned by (Dahl and Stevenson, 2010), who derived theoretical models to account for the turbulent erosion of iron diapirs via Kelvin–Helmholtz and Rayleigh–Taylor mechanisms. The main result of their study is that large diapirs (*i.e.*, of radius > 10 km) can survive complete erosion and preserve most of their initial volume as they reach the bottom of a ~ 1000 km thick magma ocean, therefore leading to metal–silicate disequilibrium.

A comparison between these different studies is not necessarily straightforward because the underlying assumptions, the governing parameters, their ranges of variation, and to some extent the geometry and modeling approaches may be very different. For instance in Rubie et al. (2003) the authors derive a conceptual/parameterized model where the criterion used to determine the diapir stable sizes was based only on the value of the Weber number, implying that viscous effects are negligible. In Ichikawa et al. (2010) surface tension and viscous effects are taken into account, however, due to computational limitations of numerical experiments, the explored range of Reynolds numbers was restricted to low values and the effect of surface tension forces on diapir breakup and stable sizes was not investigated systematically, since the Weber number was fixed to a constant value close to unity. In addition, most of their exploration was performed in a 2D Cartesian geometry, also due to limitations imposed by computational run time. On the other hand, using theoretical turbulent modeling Dahl and Stevenson (2010) have focused only on diapirs where Reynolds and Weber numbers are both very large. Although they account for moderate diapir deformation, they made the assumption that iron diapirs do not breakup during their descent through the silicate magma ocean. In a recent study, Deguen et al. (2011) have investigated experimentally the mixing of dense bodies during their sinking. They find that large bodies are not fully mixed by turbulent instabilities, which confirms qualitatively the theoretical results of Dahl and Stevenson (2010). However, in their work sinking iron bodies are modeled as a cloud of dense particles/flakes instead of a continuous body. While collective behavior within particle clouds can occur at high Reynolds numbers, it is not clear whether the dynamics and the fragmentation processes are identical for particle clouds and for initially continuous bodies.

To clarify these discrepancies, I have conducted a series of numerical simulations and theoretical calculations to derive the conditions and the timing for the breakup of axisymmetric metal diapirs of any size, sinking through a silicate magma ocean with a large range of plausible viscosity values. The corresponding range of governing parameters covers more than 16 orders of magnitude. The obtained breakup criterion is used to derive stable diapir sizes and their ability to equilibrate chemically with the surrounding silicates.

The paper is organized as follows: the next section, Section 2 introduces the fluid dynamic problem, the corresponding governing parameters and their plausible ranges. Section 3 presents a simple analytical model to derive the general kinematics of iron diapirs sinking through a magma ocean in the absence of diapir breakup. This is followed by Section 4 devoted to the dynamics of diapir fragmentation, where general criteria for diapir breakup and the corresponding timing for breakup is derived using numerical experiments, scaling analysis and analytical theory. In the last section, Section 5, preceding the conclusion, the fluid dynamics results are applied to evaluate the ability of iron diapirs to equilibrate with the surrounding silicate magma ocean during their descent.

2. Governing parameters, parameter ranges and dynamic regimes

A main focus of this study is to constrain the size of iron bodies of density ρ_m sinking through a liquid silicate magma ocean of density ρ_s and viscosity η at a given velocity v , as sketched in Fig. 1. The iron diapirs are assumed to be initially spherical with a radius R_0 , and are subject to surface tension forces acting at the interface to preserve a constant curvature κ . In principle, one should expect the diapir viscosity to be smaller than the surrounding silicate, however it is assumed here that there are no viscosity differences between the diapir and the silicates. This simplification should not affect the results and conclusions significantly.

With such a configuration the dynamics is entirely governed by two dimensionless numbers. The Reynolds number, which expresses the importance of inertia over viscous effects:

$$Re = \frac{\rho_s v R_0}{\eta}, \quad (1)$$

and the Weber number, which measures the importance of inertia over surface tension forces acting on the diapir surface:

$$We = \frac{\rho_s v^2 R_0}{\sigma}, \quad (2)$$

where σ is the coefficient of surface tension.

The value of Re defines three dynamical regimes for the sinking diapir (*e.g.*, (Crowe et al., 1997; Lamb, 1932) and references therein):

1. $Re < 1$ corresponds to the Stokes regime of creeping flow where inertia is negligible.
2. $Re = 1 - 500$ corresponds to the intermediate regime where the influences of both inertial and viscous effects are important.
3. For larger values of $Re (> 500)$ viscous forces are negligible compared to inertia. This is called the Newton regime. Within this regime the flow around the diapir transits from laminar to turbulent at about $Re \sim 10^5$ (Fig. 2).

In the Stokes regime the diapir instantaneously reaches its terminal velocity v_s (regardless of the value of its initial velocity v_0), which is for a sphere:

$$v_s = \beta \frac{(\rho_m - \rho_s) g R_0^2}{\eta}, \quad (3)$$

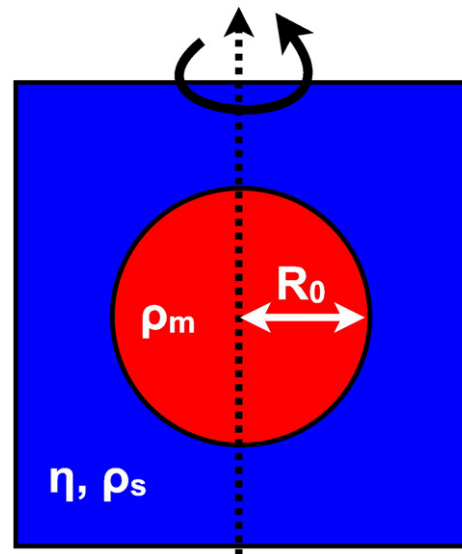


Fig. 1. Schematic representation of the problem. See text for further details.

where g is the acceleration of gravity, $\beta=2/9$ for a rigid sphere (Lamb, 1932) and $\beta=1/3$ for a frictionless sphere (Hadamard, 1911; Rybczynski, 1911). However, in the intermediate and Newton regimes the diapir accelerates or decelerates to reach its terminal velocity v_∞ given by:

$$v_\infty = \sqrt{\frac{8(\rho_m - \rho_s)gR_0}{3\rho_s C_D}} \quad (4)$$

where C_D is the coefficient of drag which will be given explicitly later. Because of this inertia, Re and We defined in Eqs. (1) and (2) become effective (or instantaneous) Reynolds and Webber numbers. For this reason it is convenient to use instead a more general definition of Re and We based on the diapir terminal velocity:

$$Re^\infty = Re \frac{v_\infty}{v} = \frac{\rho_s v_\infty R_0}{\eta} \quad (5)$$

$$We^\infty = We \left(\frac{v_\infty}{v}\right)^2 = \frac{\rho_s v_\infty^2 R_0}{\sigma} \quad (6)$$

which for a given set of physical parameters (e.g., densities, viscosity ...) have a constant value. This pair of dimensionless numbers can be revealed by carrying out dimensional analysis with the characteristic scales listed in Table 1 systematically used throughout this paper.

The values of the physical parameters appearing in Eqs. (5) and (6) are listed in Table 2. While densities, gravity and surface tension can reasonably be considered to be constant, the viscosity η and the diapir radius R_0 may vary by several orders of magnitude. As shown in Fig. 3a–b these large ranges in η and R_0 result in variations in Re^∞ and We^∞ of up to 18 orders of magnitude. Consequently, all three dynamical flow regimes mentioned earlier must be considered. One can remark, however, that all large diapirs ($R_0 > 1\text{m}$) fall in the Newton regime where viscous effects are negligible (Fig. 3a).

3. Time-dependent velocity model

In this section I present a simple analytic model to determine the sinking velocity v , the sinking distance z , and the sinking time t of a given iron diapir, starting from the most general case applying to any dynamic regime. The resulting solutions can be simplified for the Newton and the Stokes regimes. The diapir motion relative to a fixed frame of reference can be determined using Newton's law:

$$\rho_m V \frac{dv}{dt} = F_b - F_D \quad (7)$$

where $V=4\pi R_0^3/3$ is the spherical diapir volume, $F_b = V(\rho_m - \rho_s)g$ is the buoyancy force and $F_D = \rho_s \pi R_0^2 C_D v^2/2$ is the drag force opposite to the diapir motion. The drag coefficient C_D is a function of the effective diapir Reynolds number Re . I approximate such a dependence of the drag coefficient as:

$$C_D = \frac{c_s}{v} + c_N \quad (8)$$

Table 1
Characteristic scales used throughout this study.

Density	ρ_s
Distance	R_0
Velocity	v_∞
Time	R_0/v_∞

Table 2
Symbols definition and values of the physical parameters used throughout this study.

Symbol	Meaning	Range or value
R_0	Diapir initial radius	$10^{-4} - 10^5 \text{ m}$
η	Magma ocean viscosity	$10^{-4} - 10^2 \text{ Pa}$
ρ_m	Iron density	7800 kg/m^3
ρ_s	Silicate density	3750 kg/m^3
σ	Coefficient of surface tension	1 N/m
g	Acceleration of gravity	10 m/s^2
κ_c	Chemical diffusivity	$10^{-8} \text{ m}^2/\text{s}$

where $v' = v/v_\infty$ is the dimensionless sinking velocity, $c_s = 12/Re^\infty = \lim_{Re \rightarrow 0} C_D$ is the Stokes drag (Lamb, 1932) and $c_N = \lim_{Re \rightarrow \infty} C_D$ is the Newton drag, assumed to be constant and equal to about 0.3 (e.g., (Crowe et al., 1997), Fig. 2). While there are more precise approximations to C_D ((Crowe et al., 1997) and references therein), the above expression remains physically consistent for all values of Reynolds numbers. In addition, it simplifies the analytical integration of Eq. (7). The largest error in Eq. (8) with respect to the data is comparable to or smaller than uncertainties in physical parameters or uncertainties due to the fact that the sinking bodies probably do not keep a spherical shape during their descent, which can easily affect the value of the drag coefficient by 100% or more (Chang, 1961).

Non-dimensionalization of Eq. 7 with the characteristic scales listed in Table 1 yields:

$$\frac{dv'}{dt'} = \frac{3\rho_s}{8\rho_m} (C_D^\infty - v'^2 C_D) \quad (9)$$

where C_D^∞ is the drag coefficient at the dimensionless terminal velocity $v' = 1$ that according to Eq. (8) is $C_D^\infty = c_s + c_N$. Integration of Eq. (9) yields:

$$v' = \frac{1}{2c_N} \left\{ -c_s + (c_s + 2c_N) \tanh \left[\frac{\rho_s}{\rho_m} \frac{3(c_s + 2c_N)}{16} t' + \text{atanh} \left(\frac{c_s + 2c_N v'_0}{c_s + 2c_N} \right) \right] \right\} \quad (10)$$

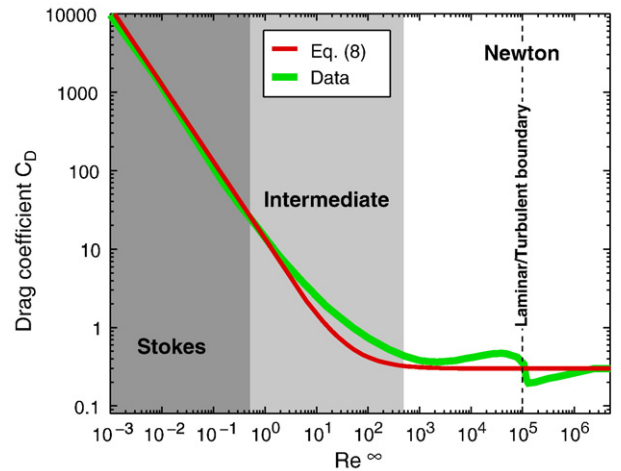


Fig. 2. Drag coefficient as a function of the Reynolds number. The red curve, corresponding to Eq. (8) is an approximate fit to the data displayed in green (Crowe et al., 1997) and references therein. Dark gray, light gray and white background colors delimit the three different dynamic regimes (Stokes, intermediate and Newton, respectively). The vertical dashed line shows the transition between laminar and turbulent flows.

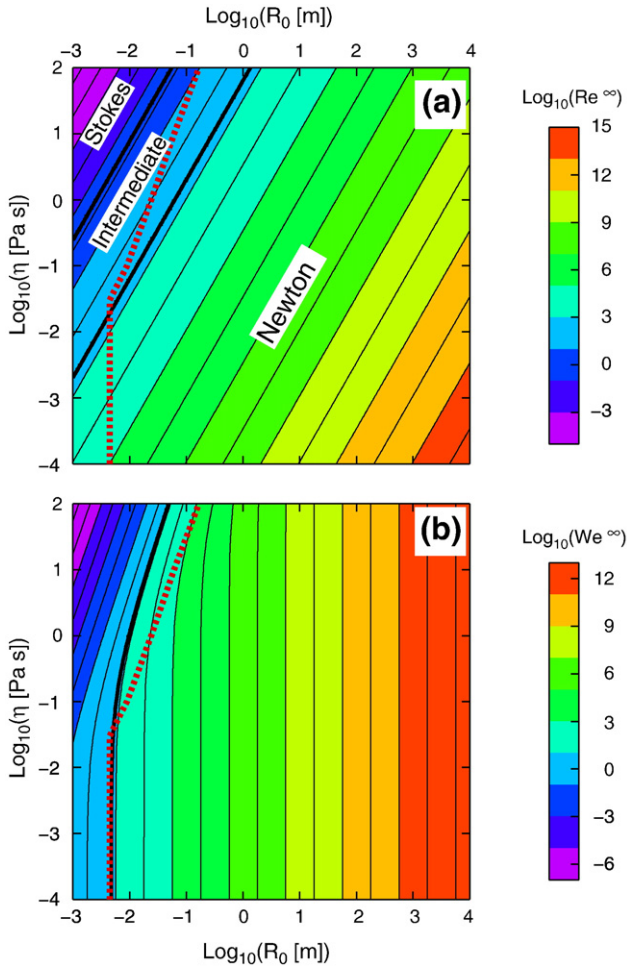


Fig. 3. Plausible range of governing parameters as a function of diapor radius R_0 and magma ocean viscosity η . Top: Reynolds number with the boundaries of the three dynamic regimes indicated by the thick black lines. Bottom: Weber number with the thick black curve indicating $We^* = 1$. The red dotted curves indicate the stable radius according to the criteria defined in Eq. (33). See text for further details.

Inverting Eq. (10) yields the sinking time as a function of the dimensionless sinking velocity:

$$t' = \frac{16}{3(c_s + 2c_N)} \frac{\rho_m}{\rho_s} \left[\operatorname{atanh} \left(\frac{2v'c_N + c_s}{c_s + 2c_N} \right) - \operatorname{atanh} \left(\frac{2v'_0c_N + c_s}{c_s + 2c_N} \right) \right]. \quad (11)$$

The dimensionless sinking distance z' is obtained by integrating Eq. (10) with respect to time:

$$\begin{aligned} z' &= z'_0 \\ &+ \left(\frac{8}{3c_N} \frac{\rho_m}{\rho_s} \right) \ln \left[\cosh \left(\frac{\rho_s}{\rho_m} \frac{3(c_s + 2c_N)}{16} t' \right) \right. \\ &\left. + \left(\frac{c_s + 2c_N v'_0}{c_s + 2c_N} \right) \sinh \left(\frac{\rho_s}{\rho_m} \frac{3(c_s + 2c_N)}{16} t' \right) \right] - \frac{1}{2} \frac{c_s}{c_N} t'. \end{aligned} \quad (12)$$

Eqs. (10), (11) and (13) are valid for any Reynolds number, but can be considerably simplified in the limit of large or small Reynolds numbers. In the Newton regime ($Re \gg 1$), $c_s \ll 1$ and the expressions for v' , t' and z' simplify to:

$$v' = \tanh \left[\frac{3}{8} \frac{\rho_s}{\rho_m} c_N t' + \operatorname{atanh}(v'_0) \right], \quad (13)$$

$$t' = \frac{8}{3c_N} \frac{\rho_m}{\rho_s} [\operatorname{atanh}(v') - \operatorname{atanh}(v'_0)], \quad (14)$$

$$z' = z'_0 + \frac{8}{3c_N} \frac{\rho_m}{\rho_s} \ln \left[\cosh \left(\frac{3c_N \rho_s}{8 \rho_m} t' \right) + v'_0 \sinh \left(\frac{3c_N \rho_s}{8 \rho_m} t' \right) \right]. \quad (15)$$

For the Stokes (low Reynolds) regime, $c_s \gg 1$, and as expected, Eq. (10) simplifies to the (dimensionless) expression of Stokes velocity: $v' = 1$.

3.1. Distance to reach essentially terminal velocity

As illustrated in Fig. 4a and b, in the intermediate and the Newton regime, the diapor reaches its terminal velocity with a certain time delay corresponding to some sinking distance $z - z_0$. One can evaluate a pseudo-terminal sinking distance defined as the distance necessary for a diapor to reach most (i.e., 99%) of its terminal velocity, or in dimensionless form: $z'_\infty = z'(v' = 0.99)$.

Fig. 4c displays z'_∞ for a range of Re^* numbers. Not surprisingly one can see that z'_∞ increases with increasing Re^* , but converges to an asymptotic maximum value (corresponding to the limit $C_d = c_N$). Assuming that the diapor is initially at rest ($v'_0 = 0$), $z'_0 = 0$, together with Eqs. (14), (15) and the definition of z'_∞ , one can calculate the maximum asymptotic value as:

$$z'_\infty^{\max} = \frac{8}{3c_N} \frac{\rho_m}{\rho_s} \ln \{ \cosh[\operatorname{atanh}(0.99)] \} \approx 36.2. \quad (16)$$

In other words all diapors reach most of their terminal velocity within a distance less than about 37 times their own radius. For a typical value of a terrestrial magma ocean thickness, say 10^3 km, only diapors larger than $\sim 10 - 100$ km still accelerate to reach their terminal velocity at the bottom of the magma ocean. On the other hand, diapors with radius less than 1 km reach their pseudo-terminal velocity within distances that are negligible compared to the thickness of a magma ocean.

4. The physics of diapor breakup

While the previous analysis focuses on describing the diapor sinking velocities and distances, it does not account for the possibility of strong diapor deformation leading to breakup. This is done in the following subsections, using numerical experiments, scaling analysis and analytical theory.

4.1. Numerical experiments

I performed a series of experiments in cylindrical axisymmetric geometry to model the evolution of an iron diapor initially spherical and at rest, gravitationally sinking through a liquid Newtonian silicate magma ocean. The dynamics is governed by three conservation equations, written below in dimensionless form (using the characteristic scales listed in Table 1). The conservation of mass:

$$\nabla \cdot \mathbf{U}' = 0, \quad (17)$$

where $\mathbf{U}' = (U'_r, U'_z)$ is the dimensionless velocity vector. The conservation of momentum:

$$\rho' \frac{D\mathbf{U}'}{Dt'} = -\nabla p' + \frac{1}{Re^*} \nabla^2 \mathbf{U}' + \frac{1}{Fr^*} C \vec{g} + \frac{1}{We^*} \kappa' \delta(d') \vec{n}, \quad (18)$$

where p is the dynamic pressure, C is the composition ranging from 0 (pure silicate) to 1 (pure iron), \vec{g} is a unit vector pointing in the direction of gravity, κ' is the dimensionless curvature of the diapor interface, $\delta(d')$ is a smeared out Dirac function (Sussman et al., 1994), d' is

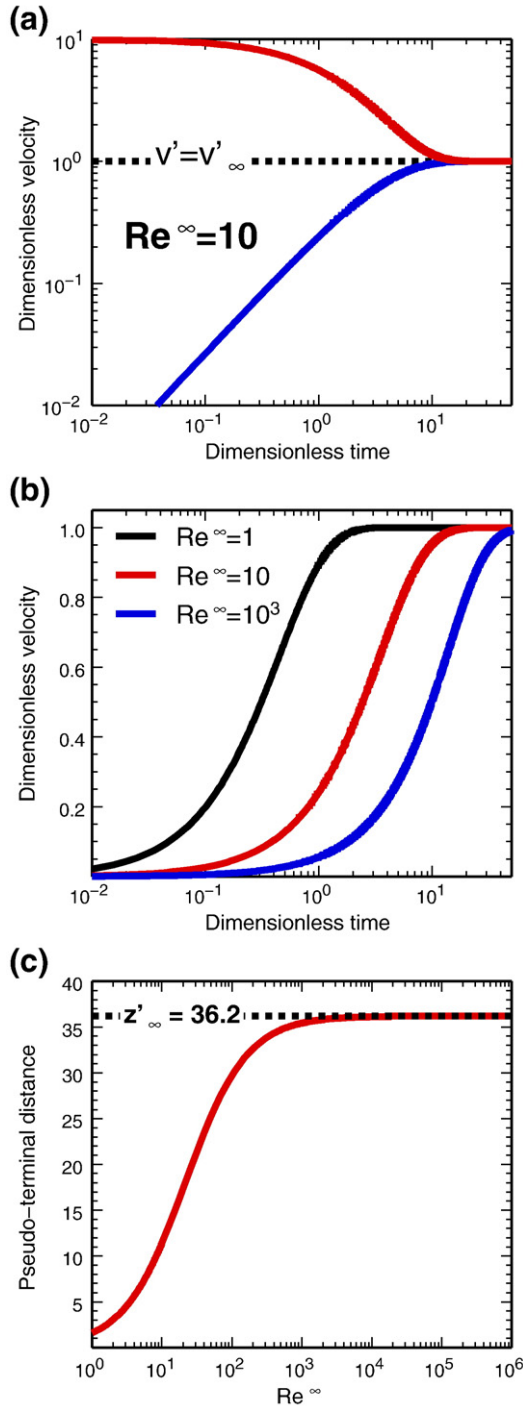


Fig. 4. Results of the time dependent sinking model. (a) Time evolution of the dimensionless diapir sinking velocity for $Re^{\infty} = 10$ with a diapir initially at rest (blue curve) or with a diapir initially sinking at a velocity equal to ten times the value of its dimensionless terminal velocity $v' = 1$. (b) Time evolution of the dimensionless diapir sinking velocity initially at rest for three values of Re^{∞} in the intermediate and Newton regimes. (c) Diapir pseudo-terminal sinking distance (*i.e.*, the distance necessary for a diapir to reach 99% of its terminal velocity as a function of the diapir Reynolds number). The black dotted line is the asymptotic value determined using Eq. (16). See Section 3.1 for further details.

the dimensionless distance to the diapir interface, \vec{n} is a unit vector normal to the diapir interface, ρ' is the dimensionless density that varies with C according to $\rho = \rho' \rho_s = \rho_s + C(\rho_m - \rho_s)$, and $F_r^s = v_s^2 / g R_0$ is a Froude number based on the Stokes velocity in Eq. 3. Similarly, R_e^s and W_e^s appearing in Eq. (18) are Reynolds and Webber numbers based on the Stokes velocity v_s rather than on the general terminal

velocity v_s , Eq. 4. These input governing parameters were chosen because in these experiments, where the diapir sinking velocity and drag coefficient are *a priori* unknowns, Re^s and We^s are output parameters and therefore their value cannot be imposed. F_r^s , R_e^s and W_e^s were adjusted in order to obtain the desired values of Re^{∞} and We^{∞} .

The last governing equation is the conservation of composition:

$$\frac{DC}{Dt'} = 0. \quad (19)$$

As previously, primes indicate dimensionless values. The mass and momentum equations are solved with a stream function formulation and are discretized with a similar approach to that described in (Kupferman, 2001). The conservation of composition is solved with a Particle Level Set method (Enright et al., 2002) as described in Samuel and Evonuk (2010). Such an approach is particularly well suited to accurately track sharp interfaces and to handle surface tension forces that can cause numerical difficulties with classical Lagrangian approaches (*e.g.*, tracer-in-cell (Samuel et al., 2010) or marker-chain (Samuel and Bercovici, 2006)). The code was successfully benchmarked against analytical and numerical solutions (Samuel and Evonuk, 2010).

The initial condition consists of a spherical diapir of dimensionless radius 1 located in the center of the axisymmetric domain (Fig. 1). Contrary to previous experiments focusing on sinking iron diapirs (Samuel and Tackley, 2008; Samuel et al., 2010), the frame of reference is located at the diapir center of mass, which allows one to model only a small area around the sinking diapir, as in Daly and Raefsky (1985). To avoid wall effects, each physical boundary is located at least 10 dimensionless units from the diapir center. The computational domain is discretized using either 200×400 square cells or 400×800 square cells for cases with the largest Reynolds numbers. All boundaries are free-slip.

In order to determine the conditions for diapir breakup I have performed a systematic exploration of the parameter space in the range $Re^{\infty} = 10^{-2} - 10^3$ and $We^{\infty} = 10^{-1} - 10^4$. Unfortunately, higher values of Re^{∞} and lower values of We^{∞} , still plausible for magma ocean scenarios (Fig. 3a–b), require higher spatial and temporal resolutions leading to prohibitive computational cost and could not be explored systematically in a timely manner. This restricted parameter range however allows the exploration of the Stokes and the full intermediate regime. A few cases were also run in the Newton regime with fairly large values of $We^{\infty} > 1$.

For each case run, the diapir initially at rest accelerates. The velocity field around the diapir organizes itself as a stagnation point flow that tends to favor the deformation of the diapir while internal motion also occurs (Fig. 5a). For cases where Re and We are relatively small, the diapir reaches its asymptotic terminal velocity with little deformation. For cases with higher Reynolds and Webber numbers, breakup occurs generally before the diapir has reached its terminal velocity. The breakup sequence occurs systematically in two steps: (1) it initiates as the diapir flattens and stretches horizontally in a pancake-like fashion due to the action of drag forces (Fig. 5b–c), (2) after a breakup distance d_b , the thickness $h(t)$ of the flattened diapir away from the rim decreases rapidly and most of the material is collected in the rim where the interface curvature (hence surface tension) is the largest, therefore forming a torus of inner radius $\sim R_b$ and a circular section with radius $\sim r_0$. A small fraction of diapir material forms a very thin film (sometimes called “bag”) with a curvature that increases with time due to the action of the external flow (Fig. 5d). This breakup sequence is also sketched in Fig. 6.

In the few experiments carried out in the Newton regime, where turbulence effects were observed, the breakup sequence was comparable to what was observed in the intermediate regime. In addition, the behavior seen in these numerical experiments and summarized in Fig. 6 is also observed in laboratory experiments between two fluids of comparable densities ((Arecchi et al., 1989) and references therein) and in laboratory experiments performed on the

fragmentation of water falling in air (Villermaux, 2007; Villermaux and Bossa, 2009), where the corresponding Reynolds numbers were much larger (*i.e.*, within the turbulent regime) than the range investigated in the most of the numerical experiments presented here. Therefore, the presence of turbulence does not appear to affect the diapir deformation and breakup sequence. As observed in these laboratory experiments, one could expect this torus to break up into spheres of radius $\sim r_0$ due to Rayleigh–Taylor or capillary instabilities. Such an asymmetric breakup cannot be observed in the present numerical experiments where axisymmetry is imposed.

Fig. 7 maps out the stable and unstable regions explored with the numerical experiments. The boundary between these regions defines

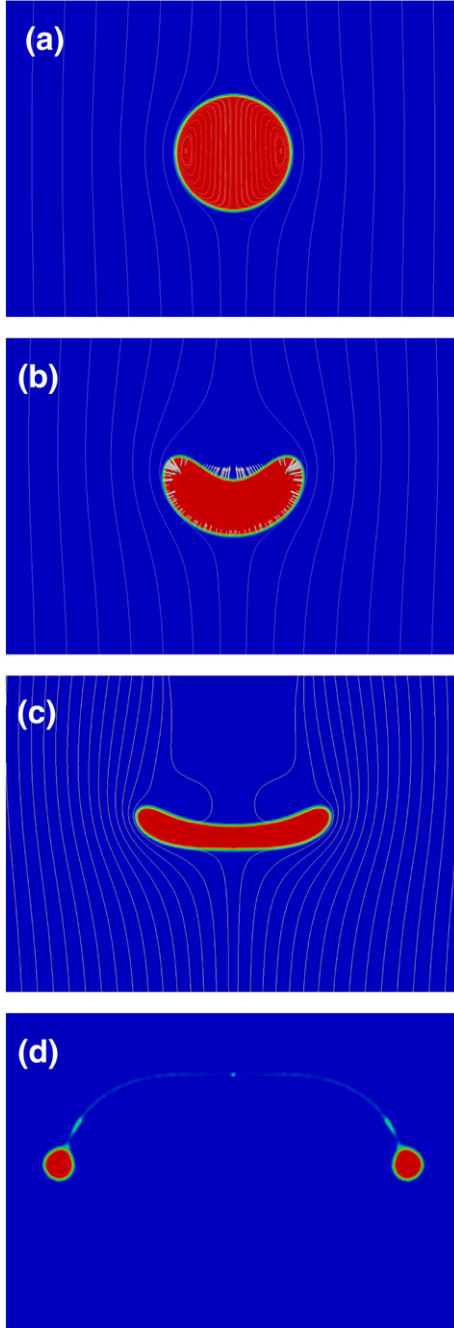


Fig. 5. Result for a numerical experiments in the intermediate regime ($Re^\infty \sim 10^2$, $We^\infty \sim 10^3$). Typical breakup sequence of an unstable iron diapir (red) initially at rest sinking through a silicate liquid magma ocean (blue) displayed in four snapshots in time. Internal and external motions are shown by streamlines in figures (a–c). The surface tension vector is displayed in snapshot b.

the experimental criterion for diapir breakup. The shape of the stable–unstable boundary can be constrained via a simple scaling analysis performed in the following subsection.

4.2. Theoretical breakup criterion: scaling analysis

Consider a spherical metal diapir of radius R_0 and surface $S = 4\pi R_0^2$ sinking through a silicate magma ocean at a given speed v . As long as the diapir preserves its initial spherical shape, and even if its sinking velocity v differs from its terminal velocity v_∞ , its acceleration with respect to the moving frame of reference located at the diapir center of mass is essentially zero. In this case, applying Newton's law with this mobile frame of reference yields the following force balance:

$$F_v + F_\tau = F_D. \quad (20)$$

The left hand side of Eq. (20) represents the two forces that prevent breakup: the diapir resistance to viscous deformation $F_v \sim \eta v S/R_0$ and the surface tension force $F_\tau \sim \sigma \kappa S$, where the spherical diapir's interface curvature κ is initially $1/R_0$. At equilibrium, these forces are balanced by the drag force $F_D \sim \rho_s v^2 S C_D$ that favors diapir deformation and breakup at high speeds.

Rewriting Eq. (20) more explicitly yields, after non-dimensionalization by the same scales used in Section 2:

$$\frac{a_1}{Re} + \frac{a_2}{We} = C_D, \quad (21)$$

where a_1 and a_2 are scaling constants accounting for geometrical factors, ignored in this dimensional analysis, which will subsequently be determined.

Using the form of drag described in Eq. (8) one can easily see that in the Stokes regime ($Re \ll 1$), viscous forces are always balanced by the drag, therefore the diapir deformation is small and no breakup should occur, even in the absence of surface tension (*i.e.*, $We \rightarrow \infty$). In that case the balance between F_v and F_D yields $a_1 = c_s Re^\infty = 12$. For larger values of Reynolds numbers (intermediate or Newton regimes) the form of drag changes (Fig. 2) and may lead to an imbalance between stabilizing forces (F_v and F_τ) and the drag force F_D . Therefore in that case, there exists a critical velocity v_c at which $F_v + F_\tau < F_D$. By Newton's law this force imbalance is compensated by an acceleration of the diapir occurring through its deformation. This marks the start of the diapir breakup sequence described in Section 4.1 and Figs. 5 and 6. Using Eqs. (5) and (6) the general criteria for diapir breakup can be written as:

$$\frac{v'_c a_1}{Re^\infty} + \frac{a_2}{We^\infty} < C_D v'_c{}^2, \quad (22)$$

where $v'_c = v_c/v_\infty$ is the dimensionless critical sinking velocity at which breakup initiates. Eq. (22) can be used to determine the critical velocity v'_c . Depending on the complexity of the form of drag chosen $C_D = f(Re, v)$ the solution v'_c may only be determined implicitly. However, as shown in Fig. 3a, large diapirs belong to the Newton regime ($Re \gg 1$) for which the drag coefficient (Eq. 8) simplifies to a constant c_N , and Eq. (22) becomes:

$$v'_c > \sqrt{\frac{a_2}{c_N We^\infty}}. \quad (23)$$

Assuming that the diapir initially at rest has reached its maximum terminal velocity $v'_c = 1$, the above criterion becomes: $We^\infty > a_2 c_N$. A similar criterion (*i.e.*, $We > 10$) was considered in (Rubie et al., 2003). Using the data displayed in Fig. 7 at $Re = 500$ (*i.e.*, the boundary between the intermediate and the Newton regime) yields a fit to the coefficients $a_2 = 7 c_N \cong 2.1$.

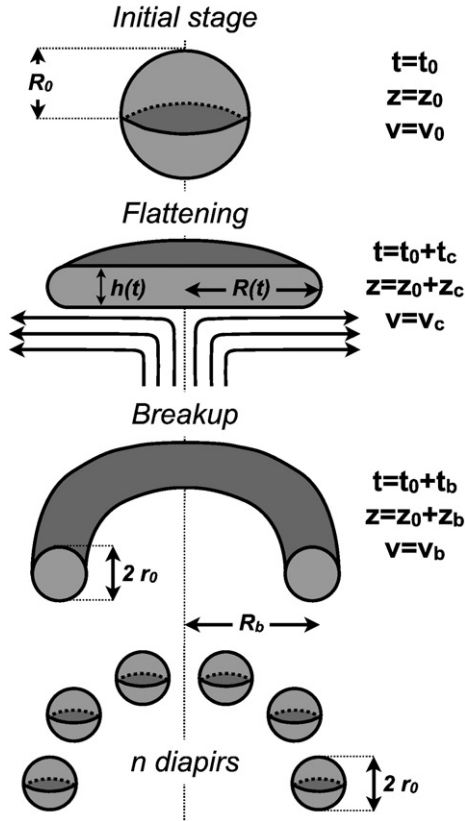


Fig. 6. Schematic diapiir breakup sequence according to the model of [Villermaux and Bossa \(2009\)](#). The breakup occurs in two stages: (1) The diapiir breakup initiation where the diapiir flattens due to the stagnation point flow developing near the front of the diapiir. (2) Breakup of the flattened diapiir into a torus of radius R_b followed up by a destabilization into smaller spherical bodies of radius r_0 .

For the intermediate regime none of the three forces in Eq. (21) can be neglected and the condition for breakup is therefore given by Eq. (22). Instead of Eq. (8) one can choose a more adapted form of drag determined by experimental fit:

$$C_d = \frac{12}{Re^\infty} + 1.05 \cdot 10^{-4} \left(\frac{1}{Re^\infty} - 1.3 \cdot 10^{-2} Re^{\infty-1/3} \right)^{-1} \quad (24)$$

which gives a better fit than Eq. (8) to the numerical experiments. Note that a direct comparison of this form of drag with the data shown in Fig. 2 would be misleading because Eq. (24) accounts for the drag of non-spherical deformable bodies while the data displayed in Fig. 2 corresponds to non-deformable rigid spheres. Using this form of drag together with Eq. (22), $v'_c = 1$, and the previously determined constants $a_1 = 12$ and $a_2 = 2.1$, yields a criteria for diapiir breakup in the intermediate regime:

$$We^\infty > 2 \cdot 10^4 \left(Re^{\infty-1} - 1.3 \cdot 10^{-2} Re^{\infty-1/3} \right). \quad (25)$$

The stability criteria for all flow regimes are summarized in Table 3 and is displayed in Fig. 7, where it shows, by construction, a very good fit (green line) to the numerical experiments.

4.3. Breakup initiation distances, breakup distances and post-breakup diapiir sizes

A priori, the fact that a diapiir is unstable does not necessarily mean that it breaks up before it reaches the bottom of a magma ocean. It is

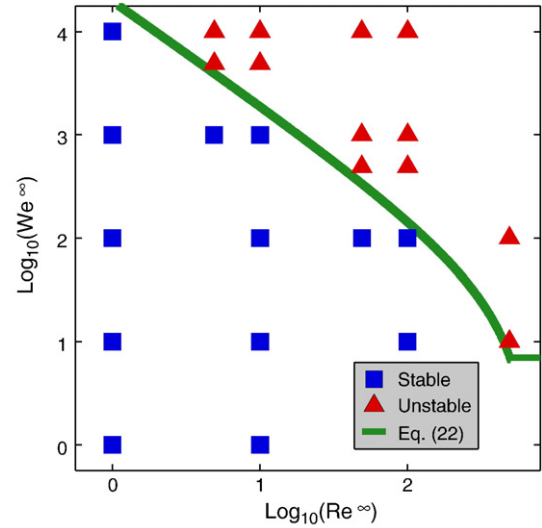


Fig. 7. Stable (blue squares) and unstable (red triangles) regions for sinking diapiirs in the (Re^∞, We^∞) space. Each symbol corresponds to a numerical experiment.

therefore important to determine the distance necessary to initiate breakup and the distance necessary for breakup to occur. In the following I consider unstable diapiirs of initial radius greater than 1 m (therefore belonging to the Newton regime), starting initially at rest at $z_0 = 0$. Using Eqs. (14) and (15) the dimensionless critical sinking distance z'_c necessary for an accelerating diapiir to reach the critical velocity v'_c to initiate breakup is:

$$z'_c = \frac{4}{3} \frac{\rho_m}{c_N \rho_s} \ln \left(\frac{1}{1-v_c'^2} \right) \quad (26)$$

Using the expression for the terminal velocity, Eq. (4), and the condition for breakup, Eq. (23), to express v'_c one gets:

$$z'_c = \frac{4}{3} \frac{\rho_m}{c_N} \ln \left[\left(1 - \frac{3}{8} \frac{a_2 \sigma}{(\rho_m - \rho_s) g R_0^2} \right)^{-1} \right] \quad (27)$$

which for values for $R_0 > 1$ m, corresponding to the Newton regime (see Fig. 3a), are much smaller than one. Consequently, in this range $z_b \ll z'_c$, therefore large, unstable diapiirs almost immediately initiate their breakup, well before they reach their terminal velocity.

Once the critical velocity is reached ($v = v_c$), the diapiir will start deforming until it breaks up over a distance, d_b (Fig. 6). To estimate this distance, one can follow the approach of [Villermaux and Bossa \(2009\)](#), which is applicable here as the assumptions made in their study also hold in the context of a terrestrial magma ocean. Assuming a stagnation point flow outside the diapiir and under the assumption that $h(t) \ll R(t)$, [Villermaux and Bossa \(2009\)](#) have shown that the

Table 3
Summary of the diapiir breakup criterion for the three flow regimes.

Flow regime	Reynolds range	Breakup criterion
Stokes	< 0.5	No breakup
Intermediate	0.5–500	$We^\infty > 2 \cdot 10^4 (Re^{\infty-1} - 1.3 \cdot 10^{-2} Re^{\infty-1/3})$
Newton	> 500	$We^\infty > 7$

dimensionless radius of the flattening pancake/cylinder (Figs. 5 and 6) evolves as:

$$R' = \exp\left(\frac{t'}{\tau'_b}\right) \quad (28)$$

where τ'_b is a dimensionless characteristic time:

$$\tau'_b = \left[\frac{\rho_s}{\rho_m} \left(-\frac{v'_c b_1}{Re^\infty} - \frac{b_2}{We^\infty} + v'_c{}^2 \right) \right]^{-\frac{1}{2}} \quad (29)$$

There are two slight differences between the above expression of the characteristic time τ'_b and the one derived in Villermaux and Bossa (2009). (1) I have included a term $-v'_c/Re^\infty$ modulated by a scaling constant b_1 that corresponds to the viscous resistance of the diapir to deformation, otherwise negligible at high Reynolds numbers. (2) The second scaling constant b_2 in Eq. (29) is absent in the derivation of Villermaux and Bossa (2009) as they explicitly prescribed a curvature at the rim of the stretching pancake $\kappa_{rim} = h/2$. While such a curvature value is probably reasonable, I chose to modulate κ_{rim} by the scaling factor b_2 of order 1 that can be constrained using a fit to the results of the numerical experiments. The last term in Eq. (29) corresponds to inertial effects that favor diapir stretching and breakup.

If $\tau'_b < 0$ no breakup occurs, the radius R oscillates with time around a mean with a decaying amplitude. However, if $\tau'_b > 0$ the disk stretches at an exponential rate and breakup occurs after a characteristic time $\sim \tau'_b$. Therefore the sign of τ'_b is also a criterion for diapir breakup, which is consistent with the scaling argument used to derive Eq. (22). To close the system in a consistent manner, one can specify the constants b_1 and b_2 by identification with Eq. (21), which yields a completely explicit expression for τ'_b :

$$\tau'_b = \left[\frac{\rho_s}{\rho_m} \left(-\frac{12 v'_c}{Re^\infty C_d} - \frac{2.1}{We^\infty C_d} + v'_c{}^2 \right) \right]^{-\frac{1}{2}} \quad (30)$$

At $t' = \tau'_b$, the rim of the disk has collected most of the diapir material gathered as a torus of exterior radius $R'_b = R'(t' = \tau'_b) = R_0 e^1$ and 'tubular' radius r_0 whose volume is: $2 \pi^2 r_0^2 R'_b = V$ (Fig. 6). In the simplest case the torus will destabilize via Rayleigh–Taylor mechanism, leading to the formation of n identical smaller diapirs of dimensionless radius (Fig. 6):

$$r'_0 = \sqrt{\frac{2}{3 \pi e^1}} \approx 0.28. \quad (31)$$

This corresponds to the formation of $n = 45$ spherical diapirs during a single breakup event, a value significantly larger than $n = 2$ considered in Rubie et al. (2003).

Since the cross sectional areas of the initial sphere and the torus are similar, it is reasonable to assume that during breakup the diapir sinking velocity remains approximately constant and equal to v_c . For large diapirs ($R_0 > 1$ m), $Re \gg 1$ and $We \gg 1$, Eq. (30) simplifies to:

$$\tau'_b = \frac{1}{v_c} \sqrt{\frac{\rho_m}{\rho_s}}, \quad (32)$$

which translates into a dimensionless breakup distance $d'_b = \sqrt{\rho_m/\rho_s} \sim 1.4$. In other words, an unstable diapir will break up within a sinking distance comparable to its own radius. This short breakup distance, which does not depend explicitly on the diapir sinking velocity, can be understood as a sinking diapir will deform at the same speed as its sinking velocity due to the stagnation point flow outside the diapir

(Fig. 5). Therefore, although larger diapirs travel faster, they will also deform and break up at a faster rate. For this reason, even iron diapirs initially sinking at a non-zero velocity (as a result of a post-impact stage) will break up within a distance close to d'_b .

4.4. Stable diapir sizes

The breakup mechanism described earlier will continue until the new diapir generation reaches a stable size (Arecchi et al., 1989; Rubie et al., 2003; Villermaux, 2007). One can determine the maximum stable size of iron bodies by solving for the radius R_0 given in Eq. (22) with $v'_c = v'_\infty = 1$:

$$\frac{12}{Re^\infty} + \frac{2.1}{We^\infty} = C_d. \quad (33)$$

Using Eqs. (5), (6), (8), and (24), the solution of Eq. (33) is displayed in Fig. 3a–b, and shows that for plausible values of magma ocean viscosities, stable diapirs belong to the intermediate and the Newton regimes. These new estimates of stable diapir sizes are also shown in Fig. 8 (solid curve) and are compared to the stable radii determined in (Rubie et al., 2003) (dashed curve). In the Newton regime both estimates are very close because the stability criteria considered are very similar. However, in the intermediate regime, contrary to Rubie et al. (2003) I consider a different breakup criterion (due to the change in drag coefficient dependence with Re). This yields larger values of diapir radius (up to about a factor of ~ 5) for large values of magma ocean viscosity than was proposed in Rubie et al. (2003).

In order to investigate the influence of these higher estimates of diapir sizes on metal–silicate equilibration processes in a magma ocean, I considered a simple chemical equilibration model described in the next section.

5. Application to metal–silicate equilibration terrestrial magma oceans

The degree of equilibration of a metal diapir sinking through a silicate magma ocean can be expressed by the diapir concentration C_m in a chemical element of interest (e.g., Ni, Co, W, Hf). Assuming that at all times t the diapir concentration is homogeneous, Fick's law is written as:

$$\frac{4\pi R_0^3}{3} \frac{dC_m}{dt} = -\frac{4\pi R_0^2}{\delta_{BL}} \kappa_c (C_m - C_{eq}) \quad (34)$$

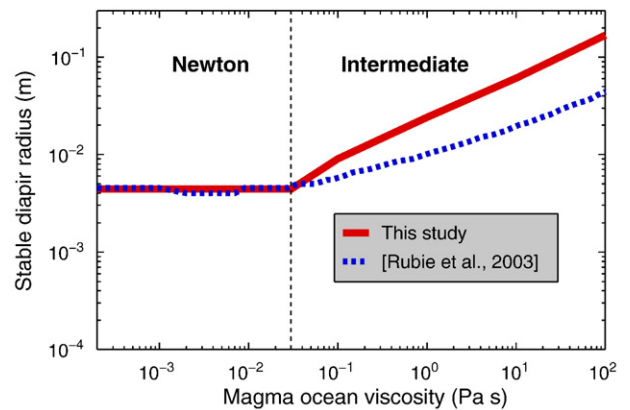


Fig. 8. Stable diapir radius as a function of plausible magma ocean viscosity spanning the Intermediate and Newton regimes. The red curve corresponds to the present study (Eq. (33)). The blue curve displays the results of Rubie et al. (2003).

with $C_{eq} = D_{ms}/C_s$ the equilibrium concentration based on the metal–silicate partition coefficient, D_{ms} , and the concentration of the element of interest in the silicates C_s . κ_c is the chemical diffusion coefficient. Assuming that C_{eq} is constant, one seeks an analytical solution to Eq. (34). Approximating the thickness of the chemical boundary layer around the sphere with $\delta_{BL} \cong \sqrt{\kappa_c} \sqrt{2 R_0/v}$ yields, after proper non-dimensionalization (with the same characteristic scales used in this paper):

$$\frac{dC_m}{dt'} = (C_{eq} - C_m) \sqrt{v' \frac{9}{2Pe}}, \quad (35)$$

where the chemical Péclet number is:

$$Pe = \frac{v_\infty R_0}{\kappa_c}. \quad (36)$$

In principle v' in Eq. (35) is a function of time t' . However, as shown in Section 3.1, stable diapirs quickly reach their terminal velocity (in less than ~ 37 diapir radii, a negligible distance compared to the thickness of a magma ocean). Therefore, for small diapir sizes, such as those shown in Fig. 8, it is reasonable to assume that $v' \sim 1$ during most of the diapir sinking. In that case taking $C_{eq} = 1$ and $C_m(t=0) = 0$, the solution of Eq. (35) is:

$$C_m = 1 - \exp\left(-t' \sqrt{\frac{9}{2Pe}}\right) \quad (37)$$

Eq. (37) gives the degree of equilibration of the diapir, ranging from 0 (complete disequilibrium) to 1 (perfect metal–silicate equilibration) as a function of dimensionless time t' . Note that the above equation ignores the presence of internal convection within the iron bodies, and the decrease of the boundary layer thickness occurring at high Reynolds number. These processes would further enhance metal–silicate equilibration (Ulvrovà et al., 2011). Therefore, the results of Eq. (37) only represent a lower bound for chemical equilibration.

Fig. 9 shows the degree of equilibration as a function of the diapir sinking distance for extreme and one intermediate value of magma ocean viscosity. In all cases, metal–silicate equilibration is essentially achieved within sinking distances less than about 2 km, which are small compared to the thickness of a magma ocean (typically few hundreds of kilometers or more). Therefore, even with the new larger estimates of stable diapir sizes displayed in Fig. 8, metal–silicate equilibration in a magma ocean is likely for all plausible values of magma ocean viscosities. In this analysis, I have considered only the stable iron diapirs that have a modest size, while much larger iron diapirs could have plunged into a silicate magma ocean (Dahl and Stevenson, 2010). However as shown in Section 4, the breakup sequence for large diapirs occurs within distances that are comparable to the initial diapir radius R_0 . In this case, the sinking distance necessary to break up an unstable diapir down to stable sizes in a cascade mechanism remains comparable to R_0 , even if several successive breakup sequences are needed (Rubie et al., 2003). Therefore for diapir sizes that are smaller than the thickness of a magma ocean (~ 1000 km) the above results should remain valid. In the case of iron diapirs of sizes greater than the thickness of the magma ocean/pond(s), despite erosion by turbulent instabilities, a significant fraction of the iron diapir survives, which would lead to chemical disequilibrium (Dahl and Stevenson, 2010). Such a scenario would correspond to giant impacts. However, as pointed out in Deguen et al. (2011), the kinetic energy of surviving iron bodies impacting the bottom of a magma ocean/pool may induce additional fragmentation and mixing that would further enhance metal–silicates equilibration.

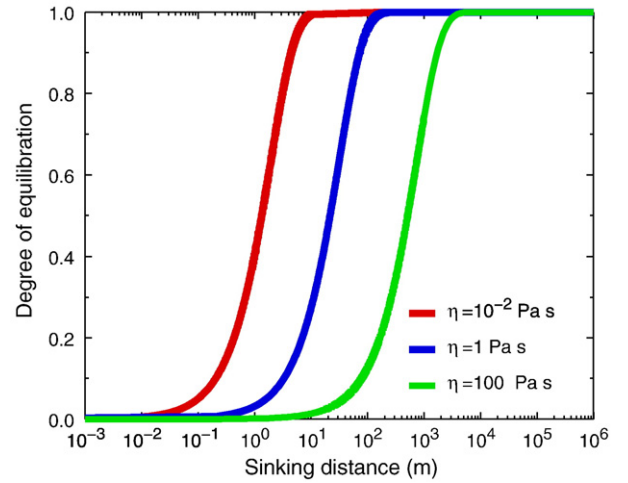


Fig. 9. Results of the equilibration model. Equilibration degree for stable diapirs for different values of magma ocean viscosities ($\eta = 0.01, 1, 100$ Pa s) as a function of the diapir sinking distance. Even for relatively viscous magma oceans (green curve), the diapir reaches high degrees of equilibration (i.e., $>99\%$) within distances smaller than 2 km, which are small compared to typical magma ocean thicknesses (~ 1000 km).

6. Conclusions

I have revisited the conditions for iron diapir breakup, and the consequences for metal–silicate equilibration in a magma ocean context. Scaling analysis combined with numerical experiments were used to derive a general criteria for diapir breakup (Eq. (22) and Table 3). Using this criteria, I have re-evaluated the sizes of stable iron bodies sinking through a silicate magma ocean (Eq. (33)). These new estimates yield stable iron radii lower than 0.2 m for plausible magma ocean viscosities.

To complement these estimates I have investigated the timing for unstable diapir breakup, using numerical experiments and analytical theory. The numerical experiments reveal the upstream formation of a stagnation point flow that favors diapir deformation at a rate proportional to the diapir sinking velocity. This behavior is also observed in laboratory experiments carried out in the turbulent regime (Villiermaux, 2007; Villiermaux and Bossa, 2009). In the context of a magma ocean, this implies that iron diapirs larger than their maximum stable size breakup within distances comparable to their initial radius into smaller size bodies. As suggested by experiments (Arecchi et al., 1989; Villiermaux and Bossa, 2009) this breakup process is repeated until the new iron bodies reach their stable sizes.

Using a simple equilibration model, I show that with such small stable diapir sizes, equilibration is achieved before the iron bodies reach the bottom of the magma ocean. These results broadly confirm the findings or the validity of several assumptions made in Ichikawa et al. (2010); Rubie et al. (2003), and contrast in part with the results of Dahl and Stevenson (2010), where the assumption that iron diapirs systematically sink without breaking up was made. However, the present study shows, on the basis of scaling analysis, numerical experiments and simple analytical theory, also consistent with laboratory experiments, that such an assumption is reasonable only if the initial iron diapir sizes are larger than the thickness of a magma ocean (e.g., as would be appropriate for a giant impact). In that case, iron diapirs would be only partially eroded by Kelvin–Helmholtz and Rayleigh–Taylor mechanisms and metal–silicate chemical exchanges would be drastically reduced (Dahl and Stevenson, 2010). Otherwise, for diapir sizes smaller than the thickness of a magma ocean, rapid breakup and metal–silicate equilibration seem unavoidable.

Acknowledgments

I am grateful to John Rudge and to an anonymous reviewer for their thoughtful comments, and I thank Dave Stevenson for

passionate discussions at the Goldschmidt conference in Prague. This work was funded by the Stifterverband für die Deutsche Wissenschaft. Figures were made with the Generic Mapping Tools (P. Wessel and W.H.F Smith, EOS, Trans. AGU 76 (1995) 329) and ParaView.

References

- Abe, Y., 1997. Thermal and chemical evolution of the terrestrial magma ocean. *Phys. Earth Planet. Inter.* 100, 27–39.
- Arecchi, F.T., Buah-Bassuah, P.K., Francini, F., Pérez-García, C., Quercioli, F., 1989. An experimental investigation of the break-up of a liquid drop falling in a miscible fluid. *Europhys. Lett.* 9, 333–338.
- Benz, W., Slatery, W.L., Cameron, G.W., 1986. The origin of the Moon and the single impact hypothesis I. *Icarus* 66, 515–535.
- Canup, R., 2004. Simulations of a late lunar-forming impact. *Icarus* 168, 433–456.
- Chang, I., 1961. On the wall effect correction of the Stokes drag formula for axially symmetric bodies moving inside a cylindrical tube. *Z. Angew. Math. Phys.* 12, 6–14.
- Coradini, A., Costanzo, F., Lanciano, P., 1983. Earth and Mars: early thermal profiles. *Phys. Earth Planet. Inter.* 31, 145–160.
- Crowe, C., Sommerfeld, M., Tsuji, Y., 1997. *Multiphase flow with droplet and particulates*. CRC Press, Boca Raton.
- Dahl, T.W., Stevenson, D.J., 2010. Turbulent mixing of metal and silicate during planet accretion – and interpretation of the Hf–W chronometer. *Earth Planet. Sci. Lett.* 295, 177–186.
- Daly, S.F., Raefsky, A., 1985. On the penetration of a hot diapir through a strongly temperature-dependent viscosity medium. *Geophys. J. R. Astron. Soc.* 83, 657–681.
- Davies, G.F., 1985. Heat deposition and retention in a solid planet growing by impacts. *Icarus* 63, 45–1968.
- Deguen, R., Olson, P., Cardin, P., 2011. Experiments on turbulent metal–silicate mixing in a magma ocean. *Earth Planet. Sci. Lett.* 310, 303–313.
- Enright, D., Fedkiw, R., Ferziger, J., Mitchell, I., 2002. A hybrid particle level set method for improved interface capturing. *J. Comput. Phys.* 183 (1), 83–116.
- Hadamard, J., 1911. Mouvement permanent lent d'une sphère liquide et visqueuse dans un liquide visqueux. *C.R. Acad. Sci.* 152, 1735–1738.
- Ichikawa, H., Labrosse, S., Kurita, K., 2010. Direct numerical simulation of an iron rain in the magma ocean. *J. Geophys. Res.* 115. doi:10.1029/2009JB006427.
- Karato, S.-I., Murthy, R.V., 1997. Core formation and chemical equilibrium in the Earth – I. Physical considerations. *Phys. Earth Planet. Inter.* 100, 61–79.
- King, C., Olson, P., 2011. Heat partitioning in metal–silicate plumes during earth differentiation. *Earth Planet. Sci. Lett.* 304, 577–586.
- Kleine, T., Rudge, J.F., 2011. Chronometry of meteorites and the formation of the Earth and Moon. *Elements* 7, 41–46.
- Kleine, T., Mezger, K., Münker, C., Palme, H., Bischoff, A., 2004a. ^{182}Hf – ^{182}W isotope systematics of chondrites, eucrites, and Martian meteorites: chronology of core formation and early mantle differentiation in Vesta and Mars. *Geochim. Cosmochim. Acta* 68, 2935–2946.
- Kleine, T., Mezger, K., Palme, H., Münker, C., 2004b. The W isotope evolution of the bulk silicate Earth: constraints on the timing and mechanisms of core formation and accretion. *Earth Planet. Sci. Lett.* 228, 109–123.
- Kokubo, E., Ida, S., 1996. On runaway growth of planetesimals. *Icarus* 123, 180–191.
- Kortenkamp, S.J., Kokubo, E., Weidenschilling, S.J., 2000. Formation of planetary embryos. In: Canup, R., Righter, K. (Eds.), *Origin of the Earth and Moon*. University of Arizona Press, pp. 85–100.
- Kupferman, R., 2001. A central-difference scheme for a pure stream function formulation of incompressible viscous flow. *SIAM J. Sci. Comput.* 23, 1–18.
- Lamb, H., 1932. *Hydrodynamics*. Cambridge Mathematical Library.
- Lin, J.-R., Gerya, T.V., Tackley, P.J., Yuen, D.A., Golabek, G.J., 2011. Protocore destabilization in planetary embryos formed by cold accretion: feedbacks from non-Newtonian rheology and energy dissipation 213, 24–42.
- Merk, R., Breuer, D., Spohn, T., 2002. Numerical modeling of ^{26}Al -induced radioactive melting of asteroids considering accretion. *Icarus* 159, 183–191.
- Monteux, J., Ricard, Y., Coltice, N., Dubuffet, F., Ulvrova, M., 2009. A model of metal–silicate separation on growing planets. *Earth Planet. Sci. Lett.* 287, 353–362.
- Monteux, J., Jellineck, A.M., Johnson, C.L., 2011. Why might planets and moons have early dynamos? *Earth Planet. Sci. Lett.* 310, 349–359.
- Ricard, Y., Šrámek, O., Dubuffet, F., 2009. A multi-phase model of runaway core–mantle segregation in planetary embryos. *Earth Planet. Sci. Lett.* 284, 144–150.
- Rubie, D.C., Melosh, H.J., Reid, J.E., Liebske, C., Righter, K., 2003. Mechanisms of metal–silicate equilibration in the terrestrial magma ocean. *Earth Planet. Sci. Lett.* 205, 239–255.
- Rubie, D.C., Nimmo, F., Melosh, H.J., 2007. Formation of Earth's core. In: Schubert, G., Stevenson, D.J. (Eds.), *Treatise on Geophysics*, Vol. 9. Elsevier, pp. 51–90.
- Rudge, J.F., Kleine, T., Bourdon, B., 2010. Broad bounds on Earth's accretion and core formation constrained by geochemical models. *Nat. Geosci.* 3, 439–443.
- Rybczynski, W., 1911. Über die fortschreitende bewegung einer flüssigen Kugel in einen Medium. *Bull. Acad. Sci. Cracov.* 1, 40–46.
- Safronov, V.S., 1978. The heating of the Earth during its formation. *Icarus* 33, 3–12.
- Samuel, H., Bercovici, D., 2006. Oscillating and stagnating plumes in the Earth's lower mantle. *Earth Planet. Sci. Lett.* 248, 90–105.
- Samuel, H., Evonuk, M., 2010. Modeling advection in geophysical flows with particle level sets. *Geochem. Geophys. Geosyst.* 11. doi:10.1029/2010GC003081 (Q08020).
- Samuel, H., Tackley, P.J., 2008. Dynamics of core formation and equilibration by negative diapirism. *Geochem. Geophys. Geosyst.* 9. doi:10.1029/2007GC001896.
- Samuel, H., Tackley, P.J., Evonuk, M., 2010. Heat partitioning during core formation by negative diapirism in terrestrial planets. *Earth Planet. Sci. Lett.* 290 13–19.
- Sasaki, S., Nakazawa, K., 1986. Metal–silicate fractionation in the growing Earth: energy source for the terrestrial magma ocean. *J. Geophys. Res.* 91, 9231–9238.
- Senshu, H., Kuramoto, K., Matsui, T., 2002. Thermal evolution of a growing Mars. *J. Geophys. Res.* 107. doi:10.1029/2001JE001819.
- Stevenson, D.J., 1990. Fluid dynamics of core formation. In: Newsom, H.E., Jones, J.H. (Eds.), *Origin of the Earth*. Oxford University Press, pp. 231–249.
- Sussman, M., Smereka, P., Osher, S., 1994. A level set approach for computing solutions to incompressible two-phase flow. *J. Comput. Phys.* 114, 146–159.
- Tonks, B.W., Melosh, J.H., 1992. Core formation by giant impacts. *Icarus* 100, 326–346.
- Tonks, B.W., Melosh, J.H., 1993. Magma ocean formation due to giant impacts. *J. Geophys. Res.* 98, 5319–5333.
- Ulvrova, M., Coltice, N., Ricard, Y., Labrosse, S., Dubuffet, F., Velimsk, J., Šrámek, O., 2011. Compositional and thermal equilibration of particles, drops, and diapirs in geophysical flows. *Geochem. Geophys. Geosyst.* 12. doi:10.1029/2011GC003757.
- Villermaux, E., 2007. Fragmentation. *Ann. Rev. Fluid Mech.* 39, 419–446.
- Villermaux, E., Bossa, B., 2009. Single-drop fragmentation determines size distribution of raindrops. *Nat. Phys.* 5, 697–702.
- Walter, M.J., Trønnes, R.G., 2004. Early Earth differentiation. *Earth Planet. Sci. Lett.* 225, 253–269.
- Weidenschilling, S.J., 1976. Accretion of the terrestrial planets II. *Icarus* 27, 161–170.
- Wood, B.J., Walter, M., Wade, J., 2006. Accretion of the Earth and segregation of its core. *Nature* 441, 825–833.